Experimental characterization of picosecond laser interaction with solid targets

D. Jung,[1,2] L. A. Gizzi,[3] L. Labate,[3] D. Neely,[1] M. M. Notley,[1] P. P. Rajeev,[1] M. Roth,[2] and G. Gregori[1,4,*]
[1]*Central Laser Facility, Rutherford Appleton Laboratory, Chilton, Didcot, OX11 0QX, United Kingdom*
[2]*Institut für Kernphysik, Technische Universität Darmstadt, Schloßgartenstrasse 9, 64289 Darmstadt, Germany*
[3]*ILIL-IPCF, Consiglio Nazionale delle Ricerche, Area della Ricerca del CNR, Via G. Moruzzi, 1-56124 Pisa, Italy*
[4]*Clarendon Laboratory, University of Oxford, Oxford, OX1 3PU, United Kingdom*
(Received 21 September 2007; revised manuscript received 9 January 2008; published 8 May 2008)

We have characterized the plasma produced by a picosecond laser pulse using x-ray spectroscopy. High-resolution high-sensitivity spectra of *K*-shell emission from a Ti plasma have been obtained, showing a strong contribution from multiply ionized ions. Hydrodynamic and collisional-radiative codes are used to extract the plasma temperature and density from these measurements. We show that our measurements can provide benchmarks for particle-in-cell (PIC) simulations of preplasma conditions in ultraintense laser-matter interactions.

DOI: 10.1103/PhysRevE.77.056403 PACS number(s): 52.38.−r, 52.38.Ph, 52.65.−y, 52.70.−m

I. INTRODUCTION

Heating of solid targets by short and ultrashort laser pulses has been under extensive investigation for many years due to its relevance in laboratory and astrophysical plasmas [1]. Independently, these studies also enable the continuous development of key applications including laser-driven sources of x rays and particle acceleration. Plasma production dynamics at subrelativistic laser intensities also plays an important role in setting preplasma conditions during ultrahigh-intensity ($I>10^{20}$ W/cm^2) interactions, where chirped pulse amplification (CPA) [2] laser pulses are commonly used. In fact, CPA pulses are often preceded by a low-intensity picosecond pedestal arising from imperfect compression of the stretched, amplified pulse. This fast pedestal is typically superimposed on a nanosecond pedestal due to fluorescence in the high-energy amplifiers of CPA lasers. In addition, lower-intensity pre- and post-pulses are also present due to the finite efficiency of techniques used to extract lower-repetition-rate pulses from high-repetition-rate oscillators and preamplifiers. The focused intensity of the pedestal or prepulses is often sufficiently high to affect properties of the target prior to the arrival of the main pulse.

These circumstances have dramatic consequences on the laser-target energy coupling that have been extensively investigated in the past two decades [3–6]. More recently, an investigation related to fast ignitor physics [7] has boosted interest in fast electron generation and energy transport into denser material [8,9]. These studies require accurate knowledge of the properties of the plasma and, in particular, of the absorption of the high-intensity laser pulse and conversion of laser energy into suprathermal electrons. In this framework, we show that the use of experimental techniques based on x-ray spectroscopy is a fundamental tool to gain information on plasma conditions.

In this paper, we describe a basic experiment aimed at a spectroscopic characterization of the picosecond laser interaction with a solid target in order to produce relevant information [10] toward a benchmarking platform for radiation hydrodynamic simulation codes and, at the same time, obtain initial plasma conditions for particle-in-cell (PIC) codes. In particular, we use inner-shell emission spectra ($n=2$ to $n=1$ transitions from both neutral and ionized atoms) from the solid material to monitor ionization and fast electron transport in the target and discuss the role of energy-coupling mechanisms in defining fast electron transport.

II. EXPERIMENTAL SETUP

The experiment was carried out at the Central Laser Facility at the Rutherford Appleton Laboratory (U.K.). In this case, 30-mJ, 15-ps, 532-nm, *s*-polarized laser pulses from a 10-Hz Continuum Leopard-D10 Nd:YAG laser system were focused on a solid titanium slab ($30\times15\times3$ mm^3) to a spot diameter of ~25 μm at a nominal intensity of 10^{14} W/cm^2. Pulses at a fundamental frequency (1064 nm, 70 mJ, 45° linearly polarized) are also used in the experiment. The target was oriented at 45° with respect to the incident beam (see Fig. 1). A highly orientated pyrolytic graphite (HOPG) crystal in 002 orientation [11,12] coupled to a Fujifilm TR2040

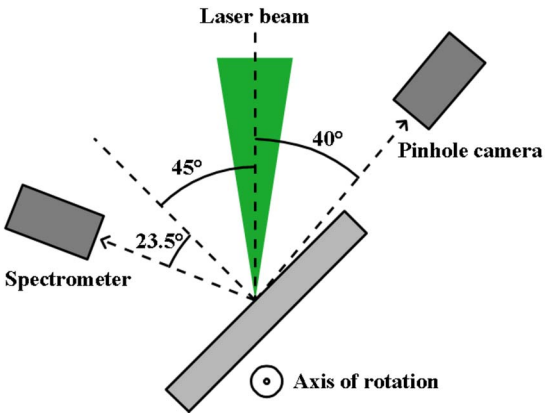

FIG. 1. (Color online) Schematic of the experimental setup: the single-photon counting CCD (not shown) is placed along the normal to the target.

*G.Gregori@rl.ac.uk

image plate detector [13] kept at 23.5° to target normal measures the Ti $K\alpha$ line emission at 4.51 keV, its satellites, and the Ti $K\beta$ line at 4.93 keV. The overall spectral resolution was $E/\Delta E \sim 350$. A broadband x-ray spectrometer [14] with a cooled charge-coupled-device (CCD) x-ray detector operating in a single-photon counting mode was also used to get information on the x-ray spectrum above 2 keV.

An x-ray pinhole camera consisting of four pinholes, each 50 μm in diameter, with a 25-μm copper aperture is positioned at an angle of 40° to the incident beam to monitor radiation temperature. The overall magnification of the camera was ~6.7. To provide spectral information in the energy range up to a few keV, different filter materials were used in each pinhole: (a) 15 μm aluminized Mylar which covers emission up to 1.5 keV, (b) 15 μm scandium to provide selection from 2.5 to 4.5 keV, (c) 5 μm aluminum to cover emission greater than 2 keV, and (d) 5 μm chromium to cover the range 2.5–6 keV. Image plates TR2040 were used as x-ray detectors, and their spectral response, as determined by Izumi *et al.* [15], was included in the analysis. To achieve good signal-to-noise ratio, taking advantage of the high repetition rate of the laser, the signal was integrated over a large number of shots. While the laser was firing, the target was continuously moved for 30 s down and for 30 s up, the same way with a velocity of ~16 μm per shot. The procedure was repeated 40 times to reach an overall integration time of 40 min. Figure 1 shows a schematic of the experimental setup. We point out here that our experiment was characterized by a partial overlapping between two consecutive shots. In the absence of any direct backscatter measurement, we speculate that a consequence of this is the loss of local target symmetry (flatness) and a reduced polarization and angular dependence of absorption [16], with a likely higher-energy coupling due to smaller losses from specular reflection.

III. ANALYTICAL MODELING

The one-dimensional (1D) radiation hydrodynamics code HELIOS [17] was used to simulate the titanium plasma. The Ti equation of state was constructed using the PROPACEOUS suite [17], which was shown to agree well with the SESAME database. The simulation was prepared with a 532-nm, 15-ps square pulse irradiating a solid foil with intensity $I=4.5\times10^{14}$ W/cm^2 and a prepulse containing 1% of the power for a duration of 0.5 ns. The prepulse profile was provided by the manufacturer for this laser system. Since the details of the spatial and temporal profiles of the plasma parameters are affected by the exact shape of the prepulse, the simulation results should only be used to infer the bulk plasma behavior and differences with the experimental values are to be expected. Figure 2 shows the spatial profiles of the electron temperature (T_e), radiation temperature (T_r), electron density (n_e), and mass density (ρ) for two different time steps: $t=0.5$ ns and $t=0.6$ ns, where $t=0.5$ ns corresponds to the start time of the main laser pulse. In the code, thermal transport is treated with a hybrid model which has a constant (solid) conductivity if $T_e<1$ eV and $\rho>1$ g/cm^3; otherwise, the regular Spitzer-Harm formula (with a flux limiter $f=0.06$) is used. HELIOS predicts a maximum radiation temperature of $T_r \sim 70$ eV and a maximum electron temperature of $T_e<150$ eV. The mass density is varying from 0.001 to 0.1 g/cm^3 in front of the target. The x-ray diagnostics are using image plates, and the measurements are thus time integrated and space integrated over the entire plasma volume. This difference must be accounted for when comparing experimental and simulated data.

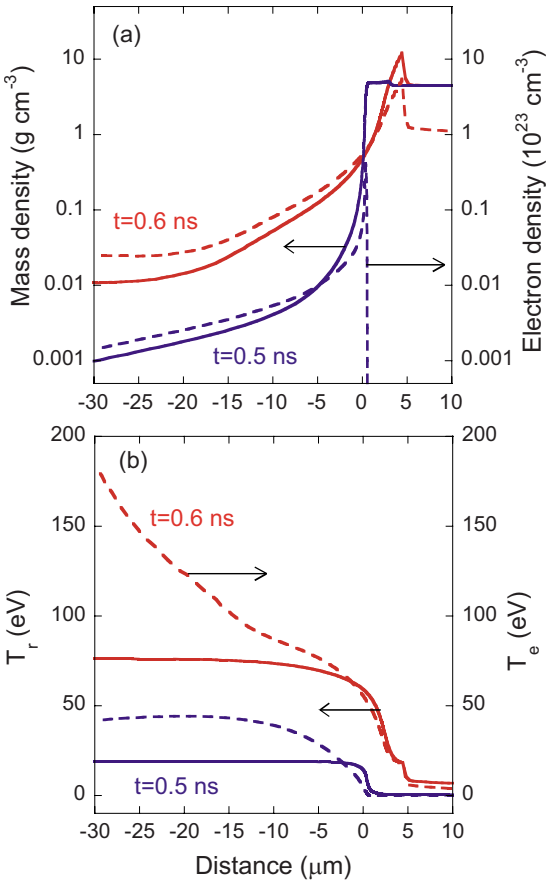

FIG. 2. (Color online) Summary of HELIOS simulation results. (a) Mass and electron densities and (b) radiation and electron temperatures. The 0 μm location corresponds to the initial position of the titanium foil which faces the laser side.

IV. EXPERIMENTAL RESULTS

Figure 3 shows the spectrum in the 2–10-keV region obtained from the single-photon counting spectrometer with the laser operating in the second harmonic. The main line is the $K\alpha$ fluorescence from Ti at 4.51 keV, with the $K\beta$ line at 4.93 keV just visible. The smaller, broad peak at approximately 3 keV is the so-called escape peak arising from fluorescence emission from the CCD silicon substrate. According to this spectrum, we can confirm that x-ray fluorescence gives a dominant contribution in the observed spectral range. The exponential fit yields a hot-electron temperature $T_{\mathrm{hot}}=1.9$ keV.

Energy calibration of the crystal (HOPG) spectrometer was performed using a target containing both a titanium and vanadium foil which allowed us to fit the position of all the

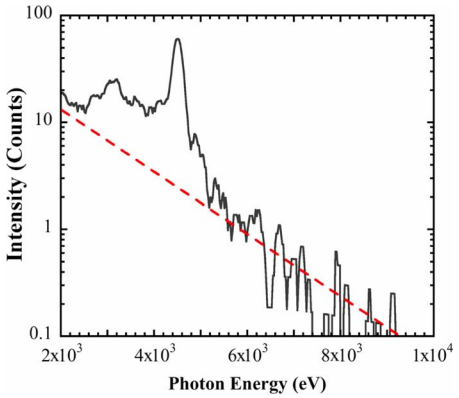

FIG. 3. (Color online) Experimental broadband x-ray spectrum obtained with the single-photon counting spectrometer. The main line is the fluorescence from Ti at 4.51 keV. The smaller broad peak at approximately 3 keV is the escape peak arising from fluorescence emission from the CCD silicon substrate. The exponential fit yields $T_{\mathrm{hot}}=1.9$ keV

Ti and V lines with a high-order nonlinear dispersion curve. Accounting for unresolved shifts in the $K\,\alpha$ lines which result from modified energy levels in partially stripped ions [9], our calibration procedure has an overall accuracy of <5 eV in the absolute position of the spectral lines.

Figure 4 shows the measured calibrated titanium spectrum at different irradiation intensities and laser wavelengths. In agreement with the single-photon counting CCD, the emission is predominantly at the $K\,\alpha$ position. All three spectra were rescaled to equal intensities of the $K\,\alpha$ lines. We clearly see that the spectra taken with 532 nm irradiation show a large number of satellites lines up to the He α line. In contrast, at 1064 nm illumination only the $K\,\alpha$ to $K\,\beta$ lines appear with a few additional satellite lines near the $K\,\alpha$ emission. The hot-electron temperature can be estimated from the scaling law $T_{\mathrm{hot}}\sim 14(I_{16}\lambda_{\mu\mathrm{m}}^2)^{1/3}T_{e,\mathrm{keV}}^{1/3}$ keV [9], where I_{16} is the intensity with units of 10^{16} W/cm^2, $\lambda_{\mu\mathrm{m}}$ is the laser wavelength in μm, and $T_{e,\ \mathrm{keV}}$ (in keV units) is the thermal electron temperature ($\sim$0.1–0.2 keV). Thus for the

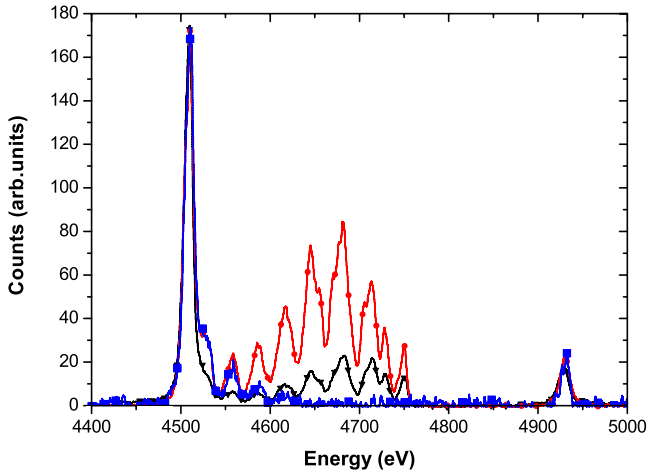

FIG. 4. (Color online) Experimental spectra taken with 1064 nm illumination at 70 mJ laser energy (circles), 532 nm with 33 mJ (inverted triangles), and 532 nm with 13 mJ (squares).

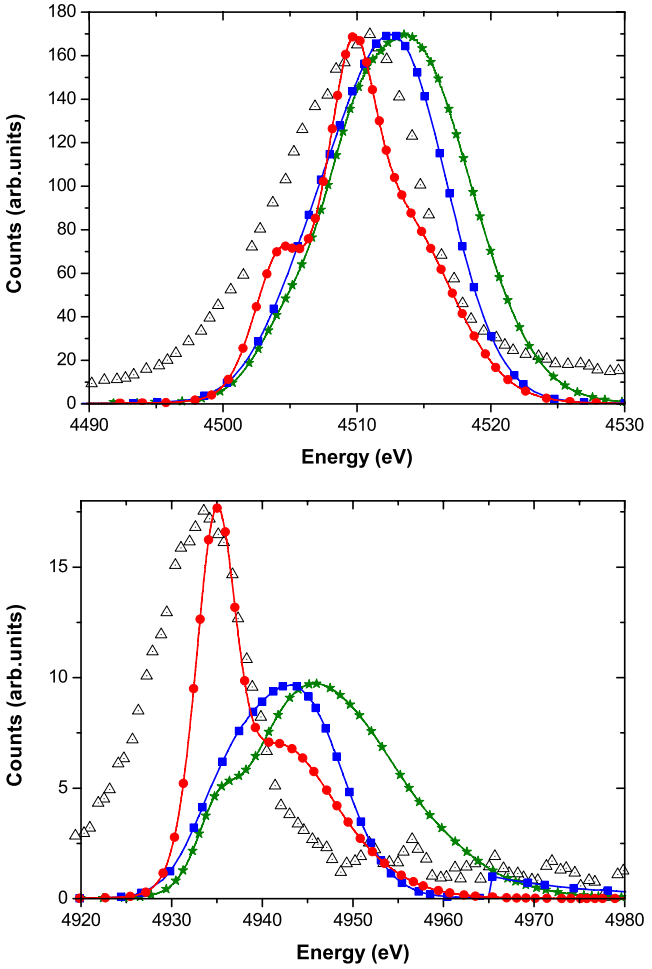

FIG. 5. (Color online) Synthetic spectra compared with experimental data for 532 nm illumination with 13 mJ laser energy (triangles) for $K\,\alpha$ (upper panel) and $K\,\beta$ lines (lower panel), with varying mass density: 0.01 g/cm^3 (circles), 4.5 g/cm^3 (squares), and 0.001 g/cm^3 (stars). The electron temperature is $T_e=12$ eV. The intensities of $K\,\alpha$ and $K\,\beta$ lines are relatively scaled.

condition of our experiment we obtain $T_{\mathrm{hot}}<2$ keV, in good agreement with the experimental observation (Fig. 3). These suprathermal electrons are likely to be injected near quarter critical density: $n_c/4\sim 10^{21}$ cm^{-3} at 532 nm or $\rho_c\sim 0.01$ g/cm^3.

The collisional-radiative code FLYCHK [18] was used to estimate plasma conditions in combination with the experimental data. Opacity effects have been accounted for using escape factors and by assuming a plasma size comparable to the spot size. Figures 5 and 6 show the calculated $K\,\alpha$ and $K\,\beta$ lines for different values for the plasma bulk electron temperature and mass density. Best agreement with the experimental data in terms of intensity ratio, line position, and linewidth is obtained by assuming that most of the inner-shell emission comes from a plasma with $T_e\sim 12$ eV and $\rho\sim 0.01$ g/cm^3. This is indeed in agreement with the radiation hydrodynamics simulations which show that at $t=0.5$ ns (i.e., at the end of the prepulse, corresponding to the time when the higher-intensity pulse arrives), $T_e\sim 10$ eV when $\rho\sim 0.01$ g/cm^3 (see Fig. 2). In the simulation we have

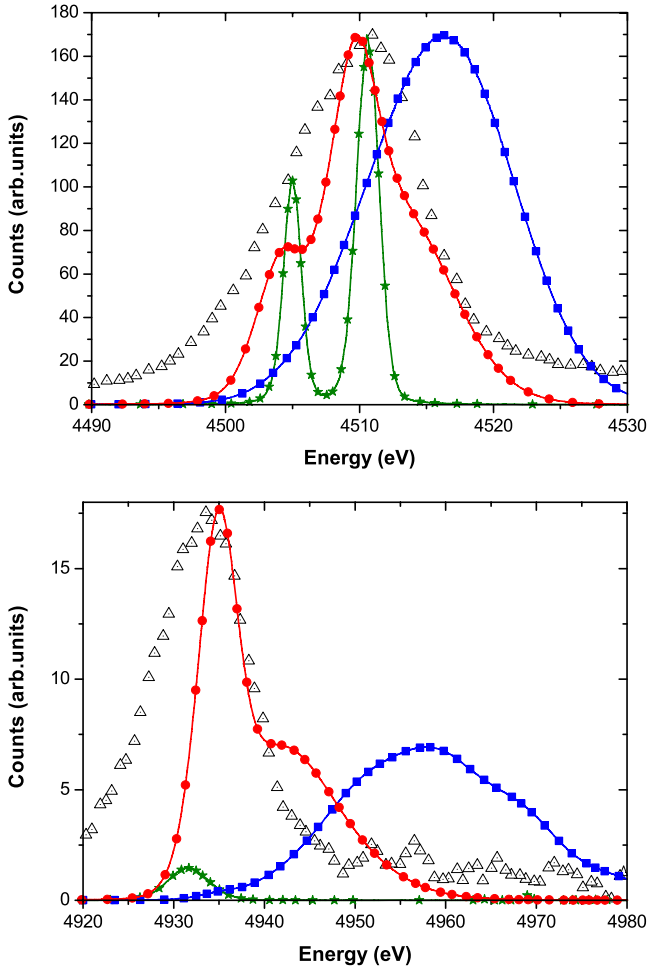

FIG. 6. (Color online) Synthetic spectra compared with experimental data for 532 nm illumination with 13 mJ laser energy (triangles) for $K\alpha$ (upper panel) and $K\beta$ lines (lower panel), with varying electron temperature: 12 eV (circles), 22 eV (squares), and 2 eV (stars). The mass density is $\rho=\rho_c=0.01$ g/cm^3. The intensities of $K\alpha$ and $K\beta$ lines are relatively scaled.

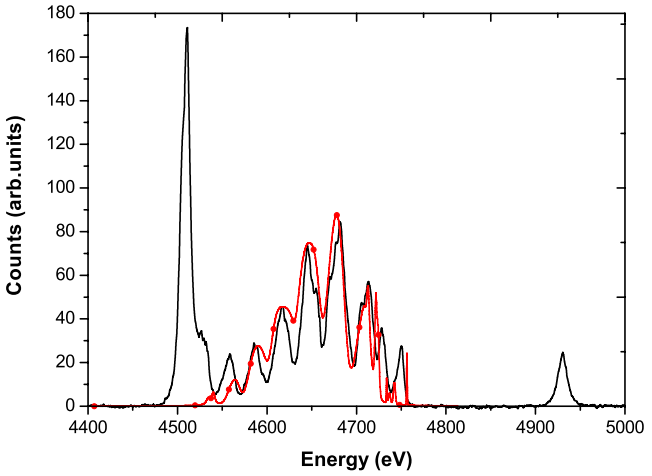

FIG. 7. (Color online) Calculated FLYCHK spectrum with $T_e=180$ eV and $\rho=0.45$ g/cm^3 (circles) compared with the experimental data (solid line).

also assumed a ~1% hot-electron fraction with $T_{\text{hot}}\sim 2$ keV. We notice that at this temperature it is the high-energy tail of the hot-electron distribution that contributes to $K\alpha$ emission. The fact that the line intensities are reproduced by the FLYCHK code only with $T_e=12$ eV and $\rho=0.01$ g/cm^3 and not with cold titanium parameters indicates that the material we are probing might be warm dense matter.

In Fig. 5 we see that good agreement between the relative intensities and position of $K\alpha$ and $K\beta$ lines is reached only by assuming that the bulk of emission is generated from a region near the critical surface. This is indeed reasonable considering that the K-shell emission is produced by inner-shell vacancies from hot-electron collisions. We have estimated the range of suprathermal electrons with energy <2 keV using the Monte Carlo code CASINO [19] and found that indeed more than 50% of their energy is deposited within 10 μm in Ti at 0.01 g/cm^3. Using the electron temperature with the scaling law $T_e\sim 1.7(I_{14}\lambda_{\mu m}^2)^{1/3}$ keV [20], we get that when the main pulse arrives, $T_e\sim 10$ eV, in agreement with FLYCHK estimates as well as HELIOS simulations (see Fig. 2).

While K-shell lines are produced by hot-electron collisions, the emission in the 4.55–4.75-keV region (see Fig. 4) is associated with thermal ionization of the titanium plasma. These are produced by inner-shell transitions in highly ionized ions up to the He-like Ti. Thermal conduction is then likely to be responsible for the transport of heat from the energy deposition layer into the higher-density layers. This is confirmed by our FLYCHK simulation as displayed in Fig. 7 where a calculated spectrum with an electron temperature of $T_e=180$ eV and a density of 0.45 g/cm^3 (10% of solid density) is compared with the corresponding experimental spectrum. As discussed in Ref. [21], the details of the hot-electron distribution are not important in determining the spectral shape of the emission from highly stripped ions. In the simulation we have then used a representative value $T_{\text{hot}}\sim 10$ keV, consistent with the fact that only higher-energy electrons in the tail of the distribution function penetrates in the higher-density regions. In addition, hot-electron relaxation times more than 10 times longer than the high-intensity laser pulse duration have been previously observed in laser plasma interaction experiments [22]. Figure 7 shows very good agreement between the experimental data and the calculated spectrum. Indeed, electron temperatures ~100 eV (or higher) are to be expected at near the solid density [21,23]. The HELIOS simulations show that at $t=0.6$ ns, the electron temperature is >50 eV at 0.45 g/cm^3. This value is slightly lower than the T_e inferred from the emission spectra. However, as pointed out above in the modeling section, these differences may be attributed to the fact that the measurements are spatially integrated. Additional uncertainty may arise from the fact that the heat transport in the simulations is modeled only with a simple flux limiter in a 1D geometry that does not account for possible nonlocal heat transport phenomena.

Additional information on the interaction conditions arises from the dependence of spectral properties upon the wavelength of the laser radiation. According to Fig. 4, the

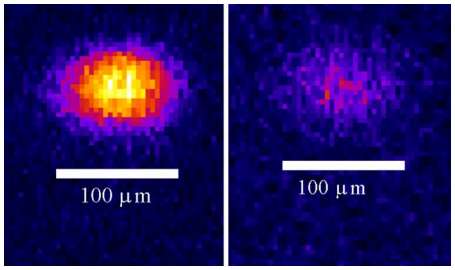

FIG. 8. (Color online) Pinhole images obtained using a 15-μm Mylar filter (right) and a 5-μm Al filter (left).

use of a longer wavelength leads to a dramatic reduction in the satellite emission. In is well known that for 1064 nm illumination, higher hot-electron temperatures and more efficient backscattering are predicted [9]. Also, due to the smaller critical density layer, absorption occurs at a larger distance from the cold, overdense target region, where collisional effects are less effective. These circumstances suggest that for the 1064-nm case there is a reduced overall coupling efficiency of the laser energy into thermal heating as well as a less efficient transport of heat in the dense plasma region and consequently a smaller fraction of highly stripped titanium ions. This is reflected by a reduction in the intensity of the satellites lines near and up to the He α line.

As a final check of the consistency of our modeling, we compare the measured radiation temperature, as obtained from differential pinhole camera imaging, with the calculated value as obtained from the HELIOS code. Pinhole images of the spot size are shown in Fig. 8. We immediately observe that according to these images, the harder x-ray emission (measured using an Al filter) is emitted by a region confined in a <25-μm spot while softer x-rays (measured with a Mylar filter) are emitted by a region which has ~ 100 μm diameter, most likely due to the contribution from the expanded coronal plasma

Moreover, as already mentioned, the four-pinhole array was differentially filtered to measure emission across several energy ranges up to a few keV. The integrated emission measured by each pinhole, F_i, was then used to extract a value for the radiation temperature of the emitting plasma by a χ^2 minimization procedure:

$$\chi^2 = \sum_{i=1}^{3} \frac{\left[F_i - A \int_0^\infty \frac{E^3}{e^{E/k_B T_r} - 1} T_i^F(E) R(E) dE \right]^2}{\sigma_i},$$

where A is a constant, T_i^F is the filter's transmission curve, R is the detector energy response [15], and σ_i is the experimental uncertainty in the data. The function χ^2 was minimized to obtain T_r (and the constant A) using a global search across a large parameter space. Figure 9 shows the radiation temperatures obtained from pinhole camera images obtained experimentally for a range of laser irradiation intensities. These results should be compared with HELIOS calculations shown in Fig. 2 that predict a maximum radiation temperature of 70 eV (see Fig. 2) for an intensity of 4.5×10^{14} W/cm^2 which is comparable to measured values.

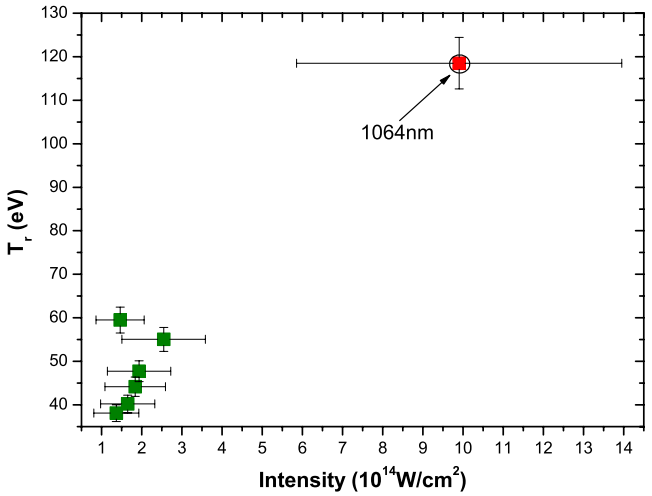

FIG. 9. (Color online) Measured radiation temperature T_r for different laser intensities with 532 nm illumination (bottom left squares) and with 1064 nm illumination (top right square).

V. CONCLUSIONS

In this work we have presented a set of experimental measurements of the interaction of a picosecond laser pulse with a solid target. Time-integrated, K-shell x-ray spectra and differential pinhole camera images were compared with collisional-radiative and radiation hydrodynamics simulation codes in order to characterize the plasma properties in terms of density and temperature. Our range of experimental results consistently indicate that x-ray emission in the K-shell spectral region consists of the superposition of two independent contributions: namely, hot-electron-driven K α emission from a relatively cold, low-density plasma and a thermal-heat-transport-driven emission from partially stripped Ti ions (shifted K α). Our findings are of relevance for a wide range of applications of short and ultrashort, intense laser pulses, including laboratory astrophysics and inertial confinement fusion research, where the results of this work are important to define the plasma conditions at the time the main pulse arrives. These results will also provide the necessary initial conditions for advanced PIC and hybrid codes and benchmarking for atomic physics codes.

ACKNOWLEDGMENTS

This work was supported by the Science and Technology Facilities Council (STFC) of the United Kingdom. We thank the Central Laser Facility Engineering and Target Fabrication groups for their support during the experiment. Useful discussions with Dr. N. Izumi at the Lawrence Livermore National Laboratory (USA) are kindly acknowledged. L.L. wishes to acknowledge financial support from the European COST action MP0601 "Short Wavelength Laboratory Sources." L.A.G. acknowledges financial support received from the STFC and from the Italian MIUR-SPARX FIRB project.

[1] B. A. Remington, R. P. Drake, and D. D. Ryutov, Rev. Mod. Phys. **78**, 755 (2006).
[2] D. Strickland and G. Mourou, Opt. Commun. **56**, 219 (1985).
[3] D. Riley *et al.*, Phys. Rev. Lett. **69**, 3739 (1992).
[4] D. Giulietti *et al.*, Phys. Rev. Lett. **79**, 3194 (1997).
[5] D. Giulietti *et al.*, Phys. Rev. E **64**, 015402 (2001).
[6] D. C. Eder *et al.*, Appl. Phys. B: Lasers Opt. **70**, 211 (2000).
[7] M. Tabak *et al.*, Phys. Plasmas **1**, 1626 (1994).
[8] P. Gibbon, *Short Pulse Laser Interactions with Matter: An introduction* (Imperial College Press, London, 2005).
[9] W. L. Kruer, *The Physics of Laser Plasma Interactions* (Westview, Boulder, CO, 2003).
[10] J. Lindl, Phys. Plasmas **2**, 3933 (1995).
[11] A. Pak *et al.*, Rev. Sci. Instrum. **75**, 3747 (2004).
[12] M. K. Urry *et al.*, J. Quant. Spectrosc. Radiat. Transf. **99**, 636 (2006).
[13] J. Miyahara *et al.*, Nucl. Instrum. Methods Phys. Res. A **246**, 572 (1986).
[14] L. Labate *et al.*, Nucl. Instrum. Methods Phys. Res. A **495**, 148 (2002).
[15] N. Izumi *et al.*, Rev. Sci. Instrum. **77**, 10E325 (2006).
[16] P. P. Rajeev *et al.*, Phys. Rev. A **65**, 052903 (2002).
[17] J. J. MacFarlane, I. E. Golovkin, and P. R. Woodruff, J. Quant. Spectrosc. Radiat. Transf. **99**, 381 (2006).
[18] H. K. Chung *et al.*, High energy density physics **1**, 3 (2005).
[19] D. Drouin *et al.*, Scanning **29**, 92 (2007).
[20] R. P. Drake, *High-Energy-Density Physics: Fundamentals, inertial fusion and experimental astrophysics* (Springer, Berlin, 2006), p. 534.
[21] S. N. Chen *et al.*, Phys. Plasmas **14**, 102701 (2007).
[22] R. G. Evans *et al.*, Appl. Phys. Lett. **86**, 191505 (2005).
[23] W. Theobald *et al.*, Phys. Plasmas **13**, 043102 (2006).